ICAS 2021 SHANGHAI
International Council of the Aeronautical Sciences
32nd Congress of the International Council of the Aeronautical Sciences
September 6-10, 2021
Pudong Shangri-La, Shanghai, China

MODELS AND METHODS FOR DRONE STRIKE LOAD PREDICTIONS

Florian Franke[1,2], Uli Burger[2], Christian Hühne[1,3]

[1]TU Braunschweig, Universitätsplatz 2, 38106 Braunschweig, Germany
[2]Technische Hochschule Ingolstadt, Esplanade 10, 85049 Ingolstadt, Germany
[3]Deutsches Zentrum für Luft- und Raumfahrt (DLR), Institut für Faserverbundleichtbau und Adaptronik,
Lilienthalplatz 7, 38108 Braunschweig, Germany

Abstract

Unmanned aerial vehicles are an increasing threat to manned aviation. Current aircraft structures are not designed to withstand mid-air collisions with drones. Since the loads in a drone strike can only be roughly estimated so far, time-consuming and cost-intensive test campaigns for a damage-resistant design must be carried out. This paper provides a new analytic model to determine the impact force during a drone strike. We superimpose the existing aircraft impact model with a spring-mass model for impacts of non-fragmenting projectile components. This leads to the new drone strike model. This model is validated with high speed impact test data and finite element simulations. A substitute structure of the drone is used to validate the model. Calculations and FEA data are in good agreement. The model is applied to a full-scale drone strike from the literature. Deviations are observed for the impact times of the individual components, due to the simplification of the drone to a 1D line model. This new analytic model can be used to determine the loads in the context of a preliminary design.

Keywords: Drone collision, Unmanned aerial vehicle, Analytic approach, Impact force, FEM

1. Introduction

Drones are a new and increasing threat to manned aviation. In addition to bird and hail strikes, drones represent a further impact load case for aircraft. There are different types of drones, from the toy drone with a few grams of maximum take-off weight (e.g. Parrot Mambo, MTOW = 73 g) to the military drone with several tons take-off weight (e.g. Global Hawk RQ-4A MTOW = 12.1 t). Due to the increase of drones within the airspace, the risk of a mid-air collision between manned aircraft and a drone increase. Statistics from different countries all over the world show, that the incidents with drones within the airspace increase. The number of incidents in Great Britain grew from 6 in 2014 to 125 in 2018 according to the UK airprox board [1].

We use the definition of a drone strike from [2]. A mid-air collision of an unmanned aerial vehicle (UAV) and a manned aircraft is a “drone strike”. A few studies about drone strikes have been published so far. Song and Schroeder [3–5] performed impact simulations of drone strikes. They compare the damage size of drone strikes on aircraft structures with damage sizes of certified bird strike tests. They conclude that drone strikes produce higher loads and larger damage. Furthermore, the flight orientation of the drone has an influence on the damage. The research group ASSURE [6–9] published four technical reports about different drone strike scenarios. They performed simulations of quadcopter and fixed wing drones colliding with different aircraft parts. Their conclusion is that drone strikes are more dangerous than bird strikes. Meng [10] et al performed impact tests on a horizontal stabilizer of a commercial airliner with a DJI (Da-Jiang Innovations Science and Technology Co., Ltd) Inspire 1 drone. The horizontal stabilizer was accelerated via a rocket sled. He concluded that a drone strike leads to a larger damage than comparable bird strikes. Lu et al [11] performed impact tests and simulations on a commercial airliner windshield with five different drone sizes. They conclude that the windshield is penetrated if the impact velocity is larger than 154.6 m/s. A distinct influence on the damage are the velocity, mass, material and configuration of the drone. Franke et al [2] present a first analytic approach to calculate the impact force of drone strikes. They compare their results with simulation data from Lu et al [11] and gain good results.

Within this paper, we verify the existing analytic model with test and simulation data from high velocity impact tests of drone components against rigid targets. We consider only drones with a MTOW below 1.5 kg, so called “small unmanned aerial vehicles” or “sUAV”. First, we describe the calculation model, the test method and a finite element model (FEM) whereas chapter 3 shows and discusses the results.

2. Models and Methods

2.1 Calculation model

The aircraft impact model (AIM) from Riera [12] is the basis of the drone strike model. Figure 1 shows this model. It was developed for the safe design of nuclear power plants against aircraft collisions and is transferred to a drone strike in [2].

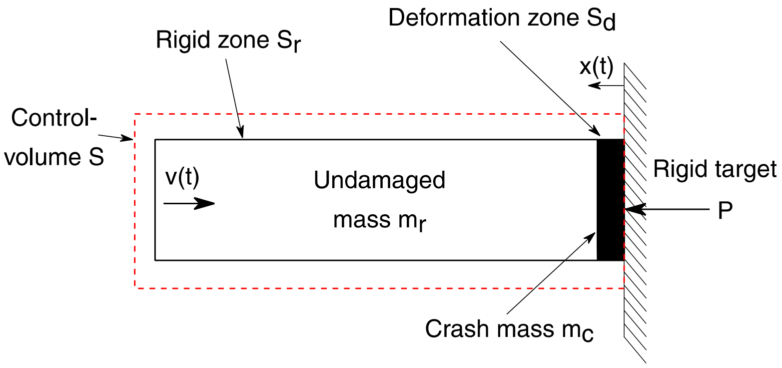

Figure 1 - Basic aircraft impact model from Riera [12]

This model divides the projectile within a control volume in two zones. The undamaged part of the projectile is perfectly rigid, whereas the crashed mass lies within the deformation zone next to the rigid target. The AIM is extended so that impact force F on inclined target structures can be calculated:

$$F(x(t)) = \left(P_c(x(t)) + \mu(x(t))\left(\frac{dx}{dt}\right)^2\right) \cdot \sin(\gamma) \cdot \cos(\zeta) \tag{1}$$

The parameter P_c is the so-called burst load, μ is the mass per unit length, γ is the inclination of the target around the y – axis and ζ is the inclination around the z – axis. This model assumes, that the crashed mass does not sum up at the interface between projectile and target.

The projectile, which consists of multiple components, is simplified to a one-dimensional line model with burst load- and mass distributions $P_c(x)$ and $\mu(x)$. The physical effect of the multi-body impact in this model is described via these distributions. We determine these distributions via reverse engineering. As quadcopter drones are able to rotate 360 degrees around their vertical axis, both distributions depend on the flight orientation α. This is the angle between one arm of the drone and the current flight direction. For simplicity, we assume for the calculations in this paper that the angle is $\alpha = 0°$. Flight orientation, mass distribution and burst load distribution for the drone model are shown in Figure 2. These distributions are used within equation (1).

The drawback of this model is that it assumes that the projectile is completely fragmented during the impact. However, tests and simulations (e. g. [7, 10, 11, 13]) show that this behavior only applies to the shell and battery. Heavy and dense components like motors mainly show plastic deformation. In order to fully describe the behavior, a new model is used at this point. We divide the drone projectile in two areas along the length being considered. Areas with components that fragment are described with the AIM. If there is a non-fragmenting component in the considered area, we superpose the AIM with a spring – mass – model for impacts. As an example, the drone in Figure 3 is divided into two areas.

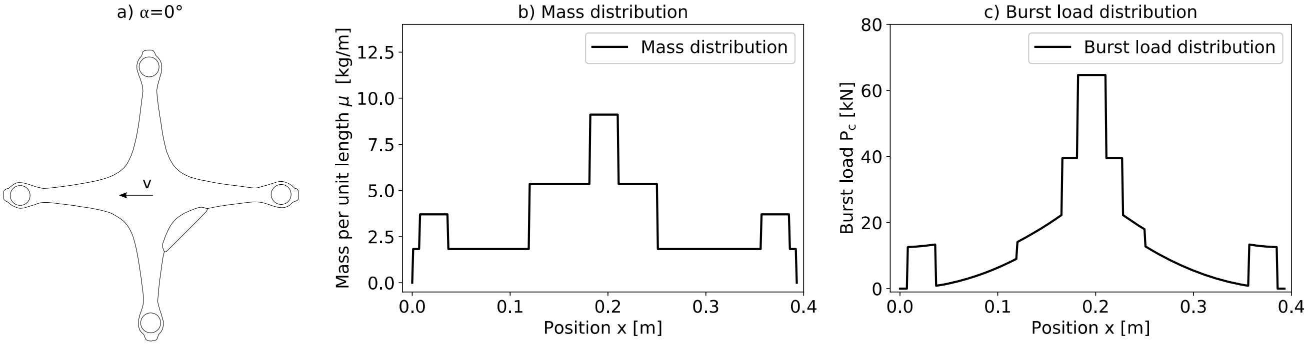

Figure 2 - a) Flight orientation, b) Mass distribution and c) Burst load distribution of drone model for the AIM

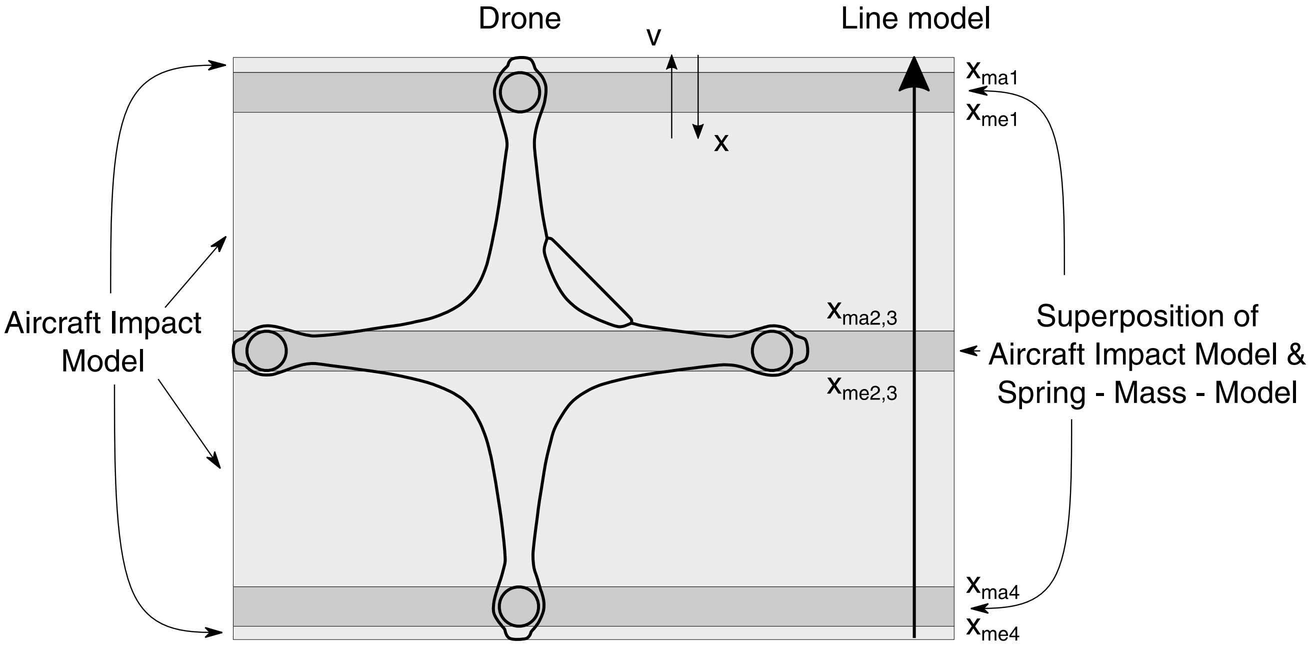

Figure 3 - Exemplary division of a drone in different areas depending on the component impact behavior

Abstracted, this results in the mechanical model shown in Figure 4. Equation (2) is the mathematical expression for this drone strike model. The areas are divided by the positions of the non-fragmenting components x_{mai} and x_{mei}.

$$F\big(x(t)\big) = \begin{cases} P_c(x(t)) + \mu(x(t))v\big(x(t)\big)^2 & x < x_{mai}; x_{mei} < x < x_{mai+1}; x_{mei+n} < x \\ P_c(x(t)) + \mu(x(t))v\big(x(t)\big)^2 + P_M(v(t), x(t)) & x_{mai} < x < x_{mei} \end{cases} \quad (2)$$

Here P_M represents the impact force from the spring – mass model. There are many different spring – mass models in the literature for the description of impacts (e. g. [14, 15]). We use a one – degree of freedom spring – mass model to determine the impact force P_M, shown in equation (3):

$$P_M = v_i \sqrt{k_e \cdot m_p} \cdot \sin\left(\frac{\pi}{T_c} \cdot t\right) \tag{3}$$

Thereby v_i represents the current velocity of the projectile, m_p is the mass of the non-fragmenting component, T_c is the contact duration and k_e is a substitute spring stiffness. Contact duration and substitute spring stiffness must be determined empirically. This formula represents a simplification of the impact of the motor. The damage and plastic deformations of the motor are modelled indirectly via the equivalent spring stiffness. The use of more sophisticated models is possible, but not part of this paper.

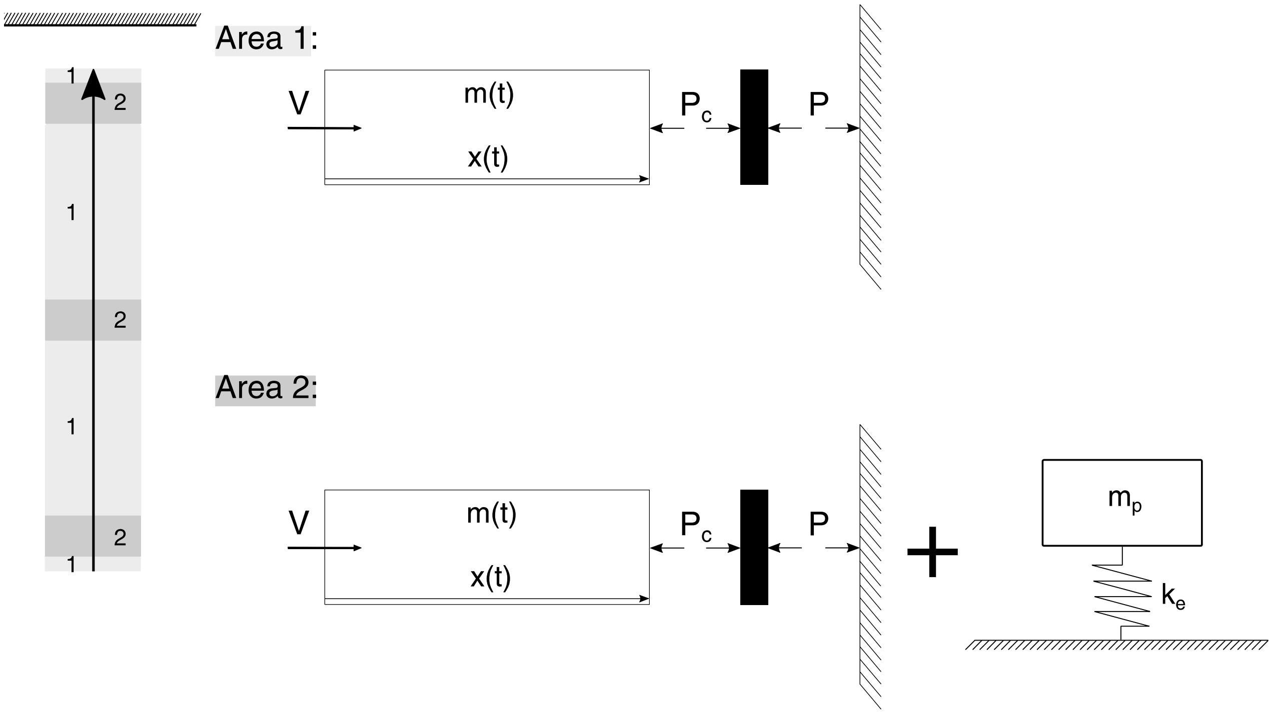

Figure 4 - Abstracted mechanical model of a drone strike

Non-fragmenting components are neglected in the mass- and burst load distribution. This leads to new curves, shown in Figure 5. We implement this model in a Python script and use the 4th order Runge – Kutta method to solve the differential equations by numerical integration. The calculation stops if $v(t) = 0\,m/s$ or $x(t) = 0\,m$ [2].

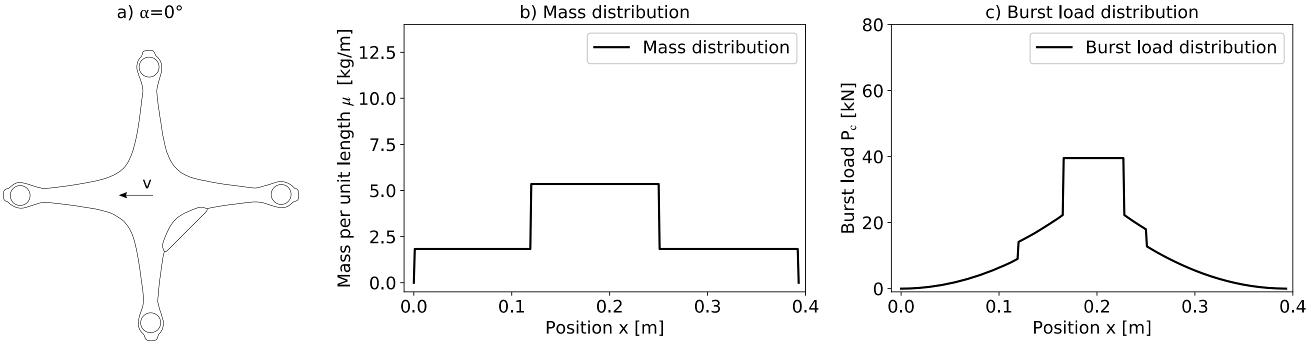

Figure 5 - a) Flight orientation, b) Mass distribution and c) Burst load distribution for the new drone strike model

2.2 Test setup

A gas gun is used for high-speed impact tests. Air is used as the gas. A pressure tank with a volume of 90 l is filled with up to 10 bar of air. The impact speed can be varied by adjusting the pressure in the tank. Via a quick-opening valve, the air escapes into an acceleration tube in which the projectile lies within a sabot. The sabot is accelerated over a distance of 5.0 m in the tube. The tube has a diameter of 50 mm. At the end of the tube, the sabot and the projectile are separated by an interceptor. The speed of the projectile is determined by light barriers. If there is sufficient energy, the target structure is penetrated, otherwise the projectile rebounds. Four piezo electronic CFW 100 kN force sensors from HBM are installed on the target structure. Each sensor is designed for a maximum load of 100 kN. The target structure is connected to the force sensors and the rigid target block via preload sets. The preload sets are tightened to 10 kN. The force sensors are connected to a charge amplifier (CMD2000). This in turn converts the charge from the force sensors into a voltage and is connected to a QuantumX MX410B measuring amplifier. Two force sensors each are picked up via one measuring amplifier. The Catman V5.13 software is used for data recording, in which the force signals are recorded synchronously. The impact process is recorded by a Photron Nova S-12 high-speed camera with 30 000 frames per second (fps). Figure 6 shows the basic structure of a corresponding test stand. We investigate impacts on a rigid wall. The target is assumed to be rigid if the deflection is less than 1% of the plate thickness at a load of 100 kN.

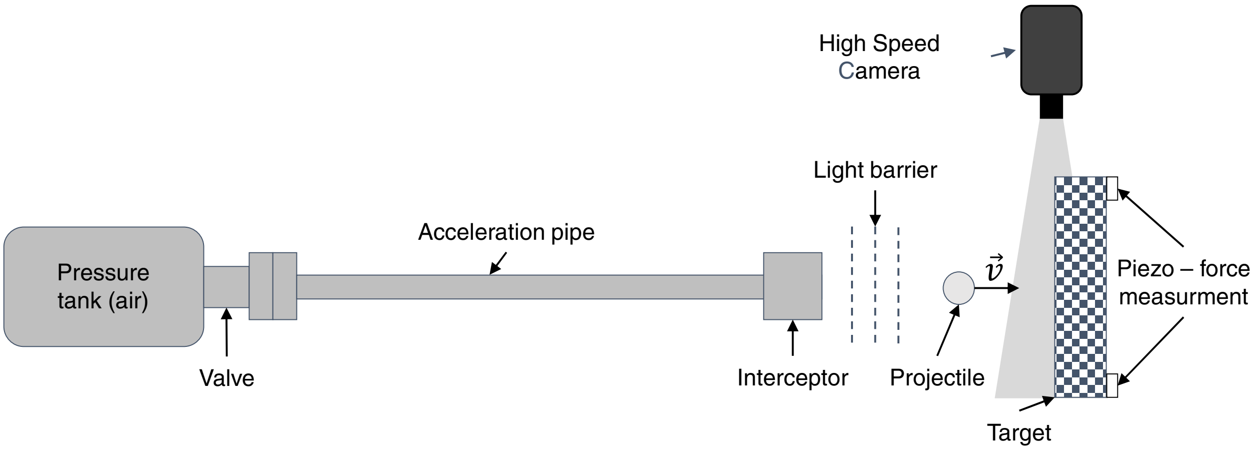

Figure 6 - Gas cannon test setup

2.3 Test specimen

The diameter of the acceleration pipe prevents the impact test of a full scale sUAV. Due to the small diameter, we use a substitute drone model to investigate the basic physical effect of a drone strike. A drone strike is a multi – body impact problem. The new drone strike model should be able to reproduce the effect of the multi-body impact. Therefore, we simplify the drone shell to a substitute structure. Non – fragmenting components can be inserted into this substitute structure. The substitute material is polylactic acid (PLA). The substitute structures are printed with a 3D printer. Figure 7 illustrates this idea of the substitute structure.

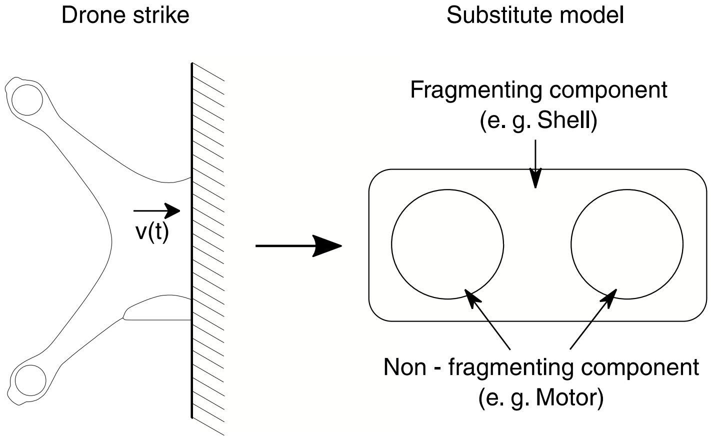

Figure 7 - Substitute structures for impact tests

Figure 8 shows the motors and the full substitute projectile. The motors of the UAV have an average diameter of 28.2 mm, a height of 36.0 mm and a weight of 53.0 g. They consist of various individual parts: Top and bottom of the housing, shaft (including ball bearing), shutter, magnets, magnetic core and the copper coil. The shutter for attaching the rotor blades is fastened with three screws. The housing of the motor is a cast aluminum (AlMg3), the iron core is modelled as steel according to AISI 4130. The coil is made of copper wire and the shaft is also made of steel. The rotors and their mountings are not considered further. The substitute structure has a length of 100 mm, a width of 40 mm and a thickness of 1.0 mm. The new drone strike model from equation (2) is validated via impact tests of this substitute structure. To apply this equation on the substitute structure, mass- and burst load distribution are needed. Both are presented in Figure 9.

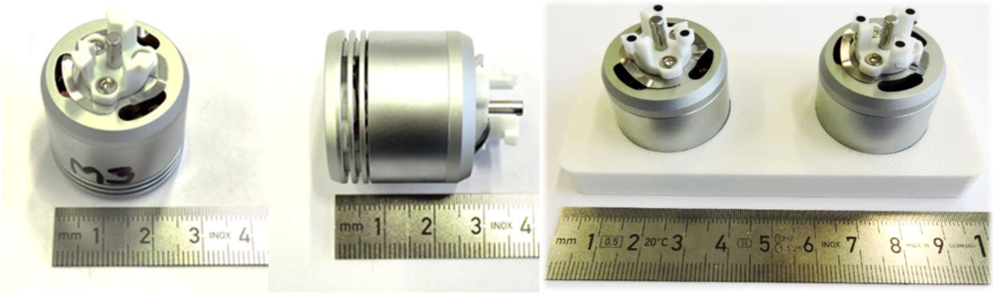

Figure 8 - Quadcopter motors with 3D printed substitute structure

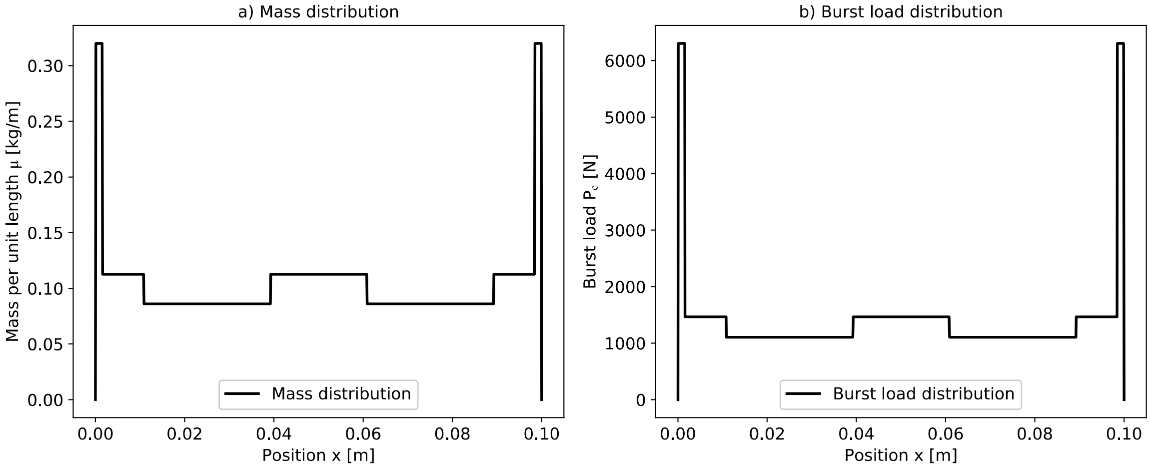

Figure 9 - Mass- and burst load distribution for the substitute structure

2.4 FE model

Finite element (FE) models allow a more differentiated analysis of the force – time curve. Therefore, we validate the simulations using the impact tests and compare the simulation data with the analytic model. The complete model (Figure 10 c) consists of two motor models (Figure 10 a) and the substitute shell model (Figure 10 b).

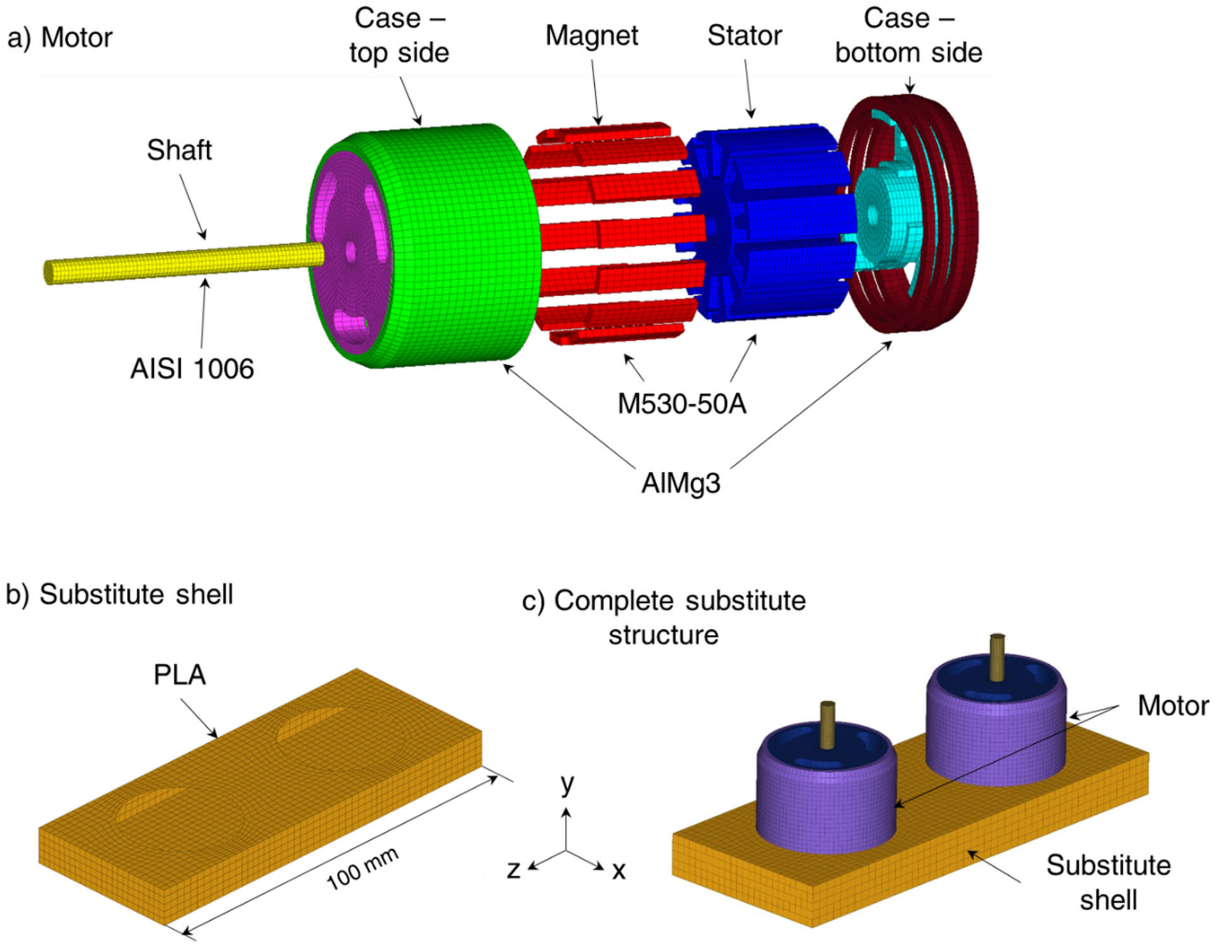

Figure 10 - FE models of test specimen: a) Motor; b) Substitute shell; c) Complete substitute structure

The motor consists of five subcomponents. Each of these subcomponents is meshed with fully integrated H8C solid elements to avoid hourglassing. The whole motor has 25056 elements. The casing is made of cast aluminum AlMg3. Stator and magnet are modeled with M530-50A steel. The shaft is an AISI 1006 steel. The copper coil is neglected, which reduces the weight of the model from 53 g to 43 g in contrast to the real motor. The substitute shell is modeled with PLA and is meshed with 16825 full integrated shell elements. The thickness of these shell elements is 1.5 mm. We use a global INTER/TYPE7 contact in Radioss. The Johnson – Cook material and damage model is used for AISI 1006 and AlMg3, as shown in Table 1.

Radioss offers the possibility that Johnson - Cook parameters are determined from yield strength, tensile strength and elongation at break internally via the program. This option is used for M530-50A with the following input parameters (Table 2). PLA has an elasto-plastic material behavior. Its material parameters were determined by quasi-static tests.

Table 1 - Johnson - Cook material and damage model parameters

	$\rho\ \left[\frac{kg}{m^3}\right]$	$E\ [MPa]$	ν	$a\ [MPa]$	$b\ [MPa]$	n	c	m	$\dot{\varepsilon}_0$	Source
AlMg3	2700	68000	0.3	28.13	278.67	0.183	0.00439	2.527	0.1	[16]
AISI 1006	7872	190000	0.3	350	275	0.36	0.022	1.0	1	[17]

	$D1$	$D2$	$D3$	$D4$	$D5$	Source
AlMg3	-0.2	1.133	-0.229	0.0897	7.978	[16]
AISI 1006	-0.8	2.1	-0.5	0.002	0.61	[17]

Table 2 - Material parameters for M530-50A and PLA

	$\rho\ \left[\frac{kg}{m^3}\right]$	$E\ [MPa]$	ν	$R_{p02}\ [MPa]$	$R_m\ [MPa]$	$\varepsilon_{max}[-]$	Source
M530-50A	7700	210000	0.3	295	430	0.89	[18]
PLA	1200	1605	0.3	15.8	31.8	0.03	-

3. Results

Impact tests are performed with the individual components motor and substitute shell. We compare the test data with analytical calculations and FEA data as shown in Figure 11. The contact force of the motor impact is determined using the spring – mass – model according to equation (3). The force of the substitute shell is determined with equation (1). We see in both diagrams, that the test data deviates from the FEA and analytic calculations. These deviations result from the measurement method. We do not measure the forces at the interface directly. The attached piezo sensors measure the complete behavior, including the structural response of the target. To determine the impact force, the decelerations of the projectile from the high-speed videos are measured. The differences between test data, FE and analytics for the motor can be explained by the fact that the impact time cannot be determined exactly from the videos. Furthermore, the damage behavior of the substitute shell prevents a determination of the deceleration and thus the impact force. The curve of the test data for the substitute shell shows significant fluctuations and is not plausible. Therefore, only FE and analytical data will be discussed in the following.

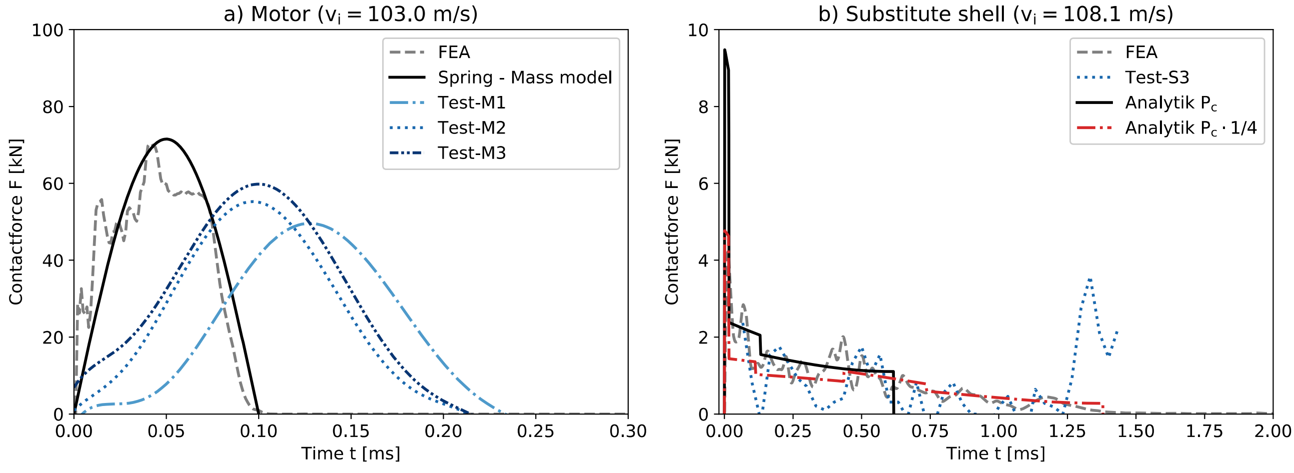

Figure 11 - Validation of single component models

As it can be seen in Figure 11 a, FEA and spring – mass model agrees well. The spring stiffness k_e is determined empirically. Its value for the calculations is k_e = 12701.2 kN/m. Qualitatively, the analytics reproduce the FEA process well. However, the FEA provides more accurate results and thus a more differentiated analysis. In contrast to the analytics, the FEA shows several load peaks. These load peaks are due to the fact the motor consists of several subcomponents. In our case, the outer shell hits the target first, but the maximum force does not occur until the steel stator impacts. Furthermore, the used spring-mass model is not able to reproduce damage, which can be seen in the FEA simulations.

The FE data and calculations of the substitute shell also show good agreement when the burst load distribution is reduced (Figure 11 b). If we use the burst load based on the yield stress of the material (Figure 9 b) we get the solid contactforce – time curve. As it can be seen, the calculation stops at t = 0.61 ms, whereas the FE simulation ends at t = 1.5 ms. If we reduce the burst load, e.g. to ¼ of its original value, the impact duration increases to t = 1.37 ms (dash dotted line). This reduces the initial load peak of 9.47 kN to 4.78 kN. In the further course of the contactforce, the difference between the two curves is at most 940 N. In relation to the course with unreduced bursting load distribution, the deviation is 39%. However, if one considers the entire system, i.e. motors and shell substitute, the influence of the burst load distribution changes accordingly. The maximum contactforce is determined by the impact of the motors. In this case it is F_{max} = 71.5 kN. The 940 N then corresponds to a difference of 1.3% and are therefore negligible. The burst load has a strong influence on the impact duration and timing, but in terms of the effect on the contactforce it is only minor.

Both components combined result in the substitute structure. A comparison of the visual deformations and damage is shown in Figure 12. The projectile has a velocity of v_i = 107.4 m/s. We compare the tests with two simulations: A perfectly vertical impact and an inclined impact according to the real test. Figure 12 shows the impact process up to 1.4 ms with images every 0.2 ms. We see that the substitute shell is very brittle and cracks are already present at t = 0.2 ms. In the simulations, the elements are deleted respectively. Due to the brittleness of the substitute shell, it is completely destroyed during the impact process. Both motors, on the other hand, are complete and show only plastic deformation. The first motor hits the target between 0 and 0.2 ms. After that, this motor bounces back. The second motor hits the first one at t = 0.4 ms. Both collide together with the rigid wall. After 0.5 ms, both motors bounce back and the rest of the replacement structure is destroyed. The difference between vertical and tilted projectile shows in the rebound. The second motor is deflected with an inclined projectile.

The analytic calculation model (equation (2)) is validated with the force – time curve at the interface between target and projectile of the FEA vertical impact. Figure 13 shows the results. An initial peak of 32.2 kN occurs within the FE results. This is not represented by the calculation model. Similar Figure 11 b, the force quickly decreases after this first peak. At time t =0.1 ms there is the impact from the first motor. FEA and calculation agree exactly at this time. Similar to Figure 11 a, deviations occur in the area of the load peak. These arise due to the damage to the projectile, which the calculation method does not model. For the impact of the second motor, an offset between FEA and calculations of Δt = 0.28 ms can be observed. This results from the fact that the second motor impacts the first motor. In the calculation model, however, it is assumed that the impact occurs at the interface between the target and the projectile and does not shift. It assumes, that components that have impacted disappear. This means that the plastic deformation of the first motor must be included in the calculation of the real impact. For the second motor, the interface is shifted by the proportion x_{plas} which corresponds to the plastic deformation of the first motor. If this proportion is added to the x-coordinate after the first impact, the curve in Figure 13 b results. FEA and calculation show the same impact point in time. Similar to the first peak, deviations occur around the peak load due to damage of the projectile. With these results, the model can be considered validated.

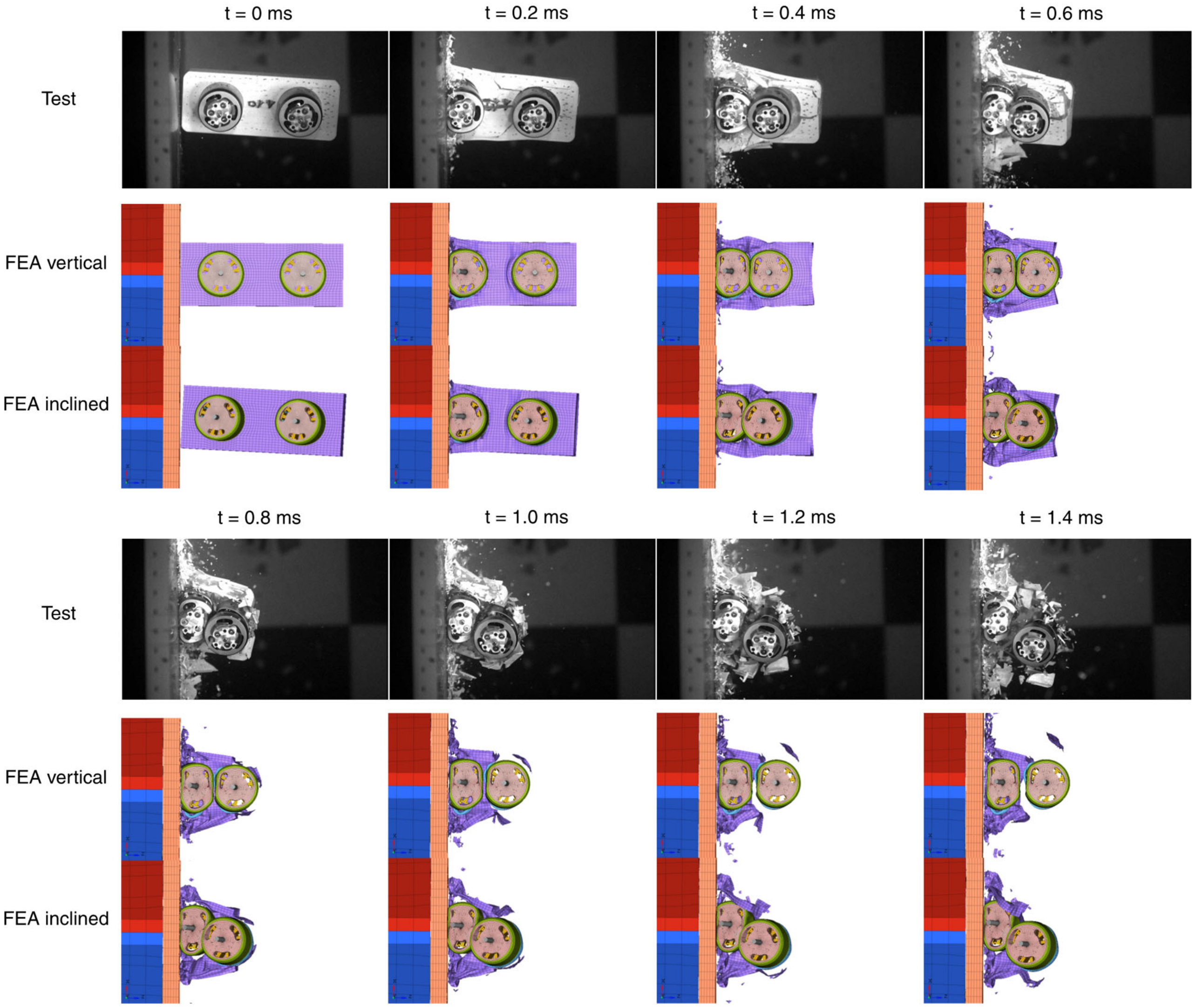

Figure 12 - Impact of the complete substitute structure in comparison to two FE simulations

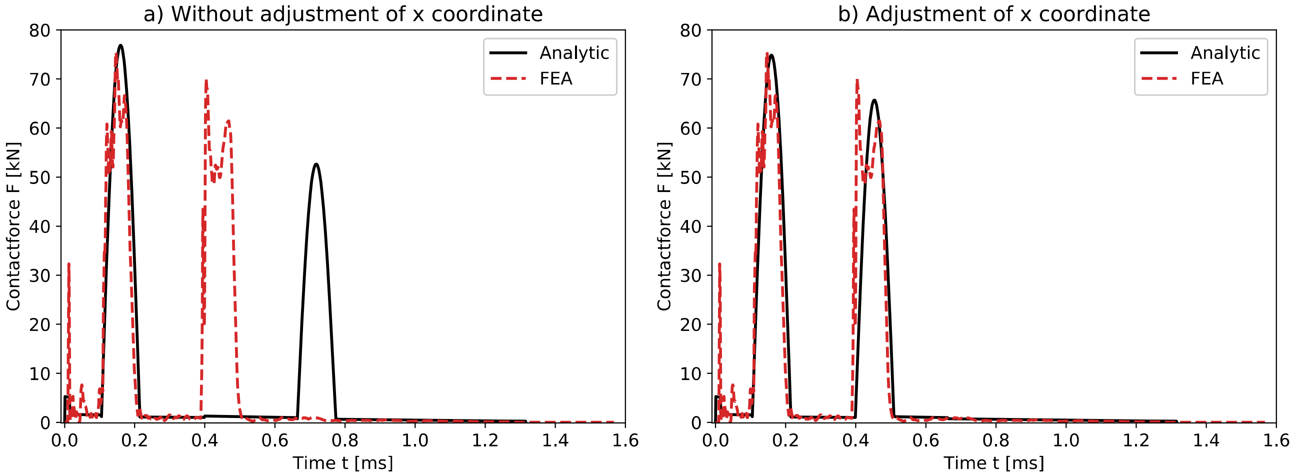

Figure 13 - Validation of calculation model with FEA data

Finally, the model is applied to a full drone strike. Reference is made to data from Lu et al [11]. They investigated a drone collision of a DJI Phantom 4 with a commercial airliner windshield. Lu et al validated their simulations with impact tests. The reference data was recorded for an impact velocity of v_i=154.8 m/s. Figure 14 shows a comparison between the new drone strike calculation model, the aircraft impact model and the FE data from Lu et al. We use the mass- and burst load distributions from Figure 5. The drone strike and aircraft impact model have an offset Δt = 0.6 ms because we neglect the rotors, which are modelled by Lu et al. It can be seen that the drone strike model and the FE data agree well. The load peak of the drone strike model is 2.5% below that of the FEA. There is an offset of 0.48 ms between the load peaks. This can be explained by simplifying the drone within the calculation method as a line model, whereas Lu et al use a full – scale drone model. The original AIM, used with input data from Figure 2, mainly shows deviations around the impacts of the motors and has a shorter impact time than the drone strike model. The model allows a first estimation of the acting contactforce during a drone strike.

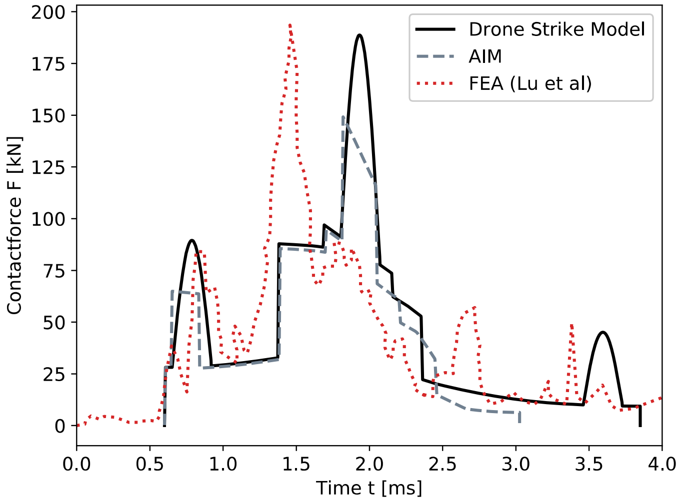

Figure 14 - Comparison of drone strike calculation model and aircraft impact model with FE data from Lu et al

4. Conclusion

This paper presents a new analytic method to determine the impact force of an sUAV collision with an aircraft. This method is validated with finite element simulations and experimental impact data. The existing aircraft impact model is superimposed with a spring-mass model for impacts of non-fragmenting drone components like motors. A substitute structure of the sUAV is being developed for validation of the analytic method. We perform impact tests with sUAV motors, the substitute shell and the combination of both. The test data, FE data and calculation results are compared with each other. We found that the new drone strike model can be applied to the impact the substitute structure. The model can also be applied to full drone strikes, as a comparison with literature data shows.

With the use of this model, it is possible to estimate the loads in the event of a drone strike in the context of preliminary design. However, the model does not allow any predictions to be made about the damage that will occur. It offers the possibility to estimate loads without complex FE simulations. Further studies need to be carried out in order to validate the calculation model for other drone models.

Acknowledgment

This research work is financed by the German Federal Ministry of Education and Research within the funding program "Forschung an Fachhochschulen" under the contract sign DESIRE – 13FH581IX6.

Contact Author Email Address

Contact author email address: Florian.Franke@thi.de

Copyright Statement

References

[1] UK Airprox Board, *Drones | UK Airprox Board.* [Online]. Available: https://www.airproxboard.org.uk /Topical-issues-and-themes/Drones/ (accessed: Jan. 7 2020).

[2] F. Franke, M. Schwab, and Burger, Uli, Hühne, Christian, “An Analytical Approach to Determine the Impact Force of Small Unmanned Aerial Vehicle Collisions with Rigid and Elastic Targets,” in *Aerospace Europe Conference 2020*, Bordeaux, 2020.

[3] Y. Song, K. Schroeder, B. Horton, and J. Bayandor, “Advanced Propulsion Collision Damage due to Unmanned Aerial System Ingestion,” in *30th Congress of the International Council of the Aeronautical Sciences*, Seoul, 2016.

[4] Y. Song, B. Horton, and J. Bayandor, “Investigation of UAS Ingestion into High-Bypass Engines, Part 1: Bird vs. Drone,” in *AIAA SciTech Forum, 58th AIAA/ASCE/AHS/ASC Structures, Structural Dynamics, and Materials Conference*: American Institute of Aeronautics and Astronautics, 2017.

[5] K. Schroeder, Y. Song, B. Horton, and J. Bayandor, “Investigation of UAS Ingestion into High-Bypass Engines, Part 2: Parametric Drone Study,” in *AIAA SciTech Forum, 58th AIAA/ASCE/AHS/ASC Structures, Structural Dynamics, and Materials Conference*: American Institute of Aeronautics and Astronautics, 2017.

[6] G. Olivares *et al.,* “Volume I - UAS Airborne Collision Severity Evaluation: Executive Summary – Structural Evaluation,” ASSURE - Alliance for System Safety of UAS through Research Excellence, 2017. Accessed: Jan. 11 2019.

[7] O. Gerardo, L. Gomez, J. Espinosa, R. Baldridge, C. Zinzuwadia, and T. Aldag, “Volume II - UAS Airborne Collision Severity Evaluation: Quadrocopter,” FAA, Springfield, UAS Airborne Collision Severity Evaluation 2, Jul. 2017. Accessed: Nov. 29 2017. [Online]. Available: http:// www.assureuas.org/projects/deliverables/a3/Volume%20II%20-%20UAS%20Airborne%20Collision%20Severity%20Evaluation%20-%20Quadcopter.pdf

[8] O. Gerardo *et al., Volume III - UAS Airborne Collision Severity Evaluation: Fixed-Wing.* [Online]. Available: http://www.assureuas.org/projects/deliverables/a3/Volume%20III%20-%20UAS%20Airborne%20Collision%20Severity%20Evaluation%20-%20Fixed-wing.pdf (accessed: Nov. 29 2017).

[9] K. D'Souza, T. Lyons, T. Lacy, and K. R. Kota, “Volume IV - UAS Airborne Collision Severity Evaluation: Engine Ingestion,” FAA, Springfield, UAS Airborne Collision Severity Evaluation, Jul. 2017. Accessed: Nov. 29 2017. [Online]. Available: http://www.assureuas.org/projects/ deliverables/a3/Volume%20IV%20-%20UAS%20Airborne%20Collision%20Severity%20Evaluation%20-%20Engine%20Ingestion.pdf

[10] X. Meng *et al.,* “Dynamic response of the horizontal stabilizer during UAS airborne collision,” *International Journal of Impact Engineering*, vol. 126, pp. 50–61, 2019, doi: 10.1016/j.ijimpeng.2018.11.015.

[11] X. Lu, X. Liu, Y. Li, Y. Zhang, and H. Zuo, “Simulations of airborne collisions between drones and an aircraft windshield,” *Aerospace Science and Technology*, p. 105713, 2020, doi: 10.1016/j.ast.2020.105713.

[12] J. D. Riera, “On the stress analysis of structures subjected to aircraft impact forces,” *Nuclear Engineering and Design*, vol. 8, no. 4, pp. 415–426, 1968, doi: 10.1016/0029-5493(68)90039-3.

[13] A. Dadouche, A. Greer, B. Galeote, T. Breithaupt, C. Vidal, and R. Gould, “Drone impact assessment on aircraft structure: windshield and leading edge testing and analysis,” CR-GTL-

2020-0054, Mar. 2020.

[14] S. Abrate, “Modeling of impacts on composite structures,” *Composite Structures*, vol. 51, no. 2, pp. 129–138, 2001, doi: 10.1016/S0263-8223(00)00138-0.

[15] R. Olsson, “Impact response of composite laminates - a guide to closed form solutions,” The Aeronautical Research Institute of Sweden, Stockholm, Jan. 1993. Accessed: Jul. 13 2020. [Online]. Available: https://www.researchgate.net/publication/331634021_Impact_response_of_composite_laminates_-_a_guide_to_closed_form_solutions

[16] M. Rodriguez-Millan, D. Garcia-Gonzalez, A. Rusinek, and A. Arias, “Influence of Stress State on the Mechanical Impact and Deformation Behaviors of Aluminum Alloys,” *Metals*, vol. 8, no. 7, p. 520, 2018, doi: 10.3390/met8070520.

[17] C. Lakshmana Rao, K. R. Y. Simha, and V. Narayanamurthy, *Applied impact mechanics*. Chichester, United Kingdom: Wiley, 2016. [Online]. Available: http://onlinelibrary.wiley.com/book/10.1002/9781119241829

[18] Cogent Power Ltd, *Electrical Steel Non Oriented Fully Processed.* [Online]. Available: https://perso.uclouvain.be/ernest.matagne/ELEC2311/T2006/NOFP.pdf (accessed: Mar. 11 2021).